Part I:

New Observations

Chapter 2

Photometric Surveys of Taurus and Upper Scorpius Using Quest-2: The Saga

Results from my thesis work center around identification and analysis of large numbers of new young and intermediate-age PMS stars in the two nearby star forming regions of Taurus and USco. This work required multiple types of observations, starting with large photometric surveys carried out using the Quest-2 camera on the Palomar 48-inch telescope. All of the new PMS stars presented in this work were first identified as candidate young objects based on their optical Quest-2 colors and magnitudes, and later confirmed from spectroscopic analysis to be bona fide PMS stars.

As part of my work with the Quest-2 data, I built a PSQL database which allowed me to easily store, organize, and access the data, and a C++/PSQL software package for data calibration and manipulation. In total, my survey consists of $UBRI$ observations of $\sim$250 deg^2 near Taurus and $\sim$150 deg^2 near USco. Twelve separate scans were observed of the entire survey field near Taurus, and 24 scans were observed of the central $\sim$60 deg^2 of the field in USco. Motivations for observing specific areas in each region are described in chapters 4 & 5. A detailed discussion of PMS star candidate selection is reserved for chapter 3. In this chapter, I describe the Quest-2 camera and give an abbreviated description of the processes required to reduce and calibrate the data.

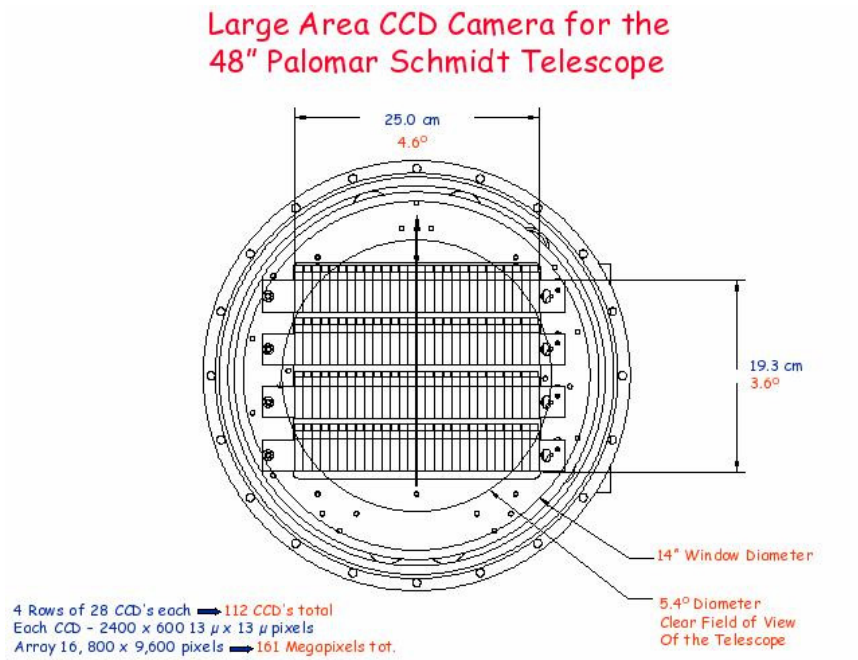

Figure 2.1 Layout of CCDs in the Quest-2 camera. Image taken from http://hepwww.physics.yale.edu/quest/large-camera.html.

2.1 Quest-2 Camera and Yale Reduction Pipeline

All photometric data were taken with the Quest-2 Camera (Rabinowitz et al., 2003) on the 48-inch Samuel Oschin Schmidt Telescope at Palomar Observatory. The Quest-2 Camera is a large-area mosaic of 112 CCDs arranged in 4 rows by 28 columns (see figure 2.1). Each of the four rows views the sky through a separate filter, in this case, UBR or I. The CCDs are 600×2400 pixels with a scale of $\sim$0.8"/pixel. In total, the camera covers a $3.6^o \times 4.6^o$ field of view, but taking into account gaps between rows and chips, the total on-sky coverage is 9.4 deg^2. The data were observed in driftscan mode in which any given patch of sky is observed over the entire 2400-pixel width of four separate CCDs (1 per filter) in one of the 28 columns. Charge is continuously read out of each CCD throughout the observation and the final data product is a strip of uniform width in declination and time-dependent length in right ascension that has been imaged in four filters.

In Taurus, one strip covering the RA range $40^o \lesssim \alpha \lesssim 90^o$ and spanning 4.6^o

in declination centered on δ=22.5^o was observed twice per night on the nights of 27–30 November 2003 and 4–5 December 2003 for a total of 12 scans of the same portion of the sky. This spatial area includes the young regions of L 1536 and L 1529, as well as the Pleiades open cluster (α=57^o, δ=24^o). In USco, three scans, centered at $\delta = -15.7^o, -19.5^o, -23.3^o$, were each observed between RA of 15h46m and 16h36m. The scan centered at $\delta = -19.5^o$ was observed 3–4 times per night on seven consecutive, photometric nights between 20 and 26 June 2004. The other two scans were observed once each during this period. The CCDs are less sensitive in the U-band than anticipated and very few source detections were obtained in either region. I therefore exclude the U data from the remainder of this discussion. In addition, 14 of the 84 B, R, I CCDs have failed since installation due to bad connections or faulty chips, rendering the spatial coverage within each survey region non-uniform.

When operated in driftscan format, the Quest-2 camera generates ~50 GB of raw, compressed data in a single night. To efficiently process such a large volume of data, the Quest-2 Collaboration (Rabinowitz et al., 2003) has developed automated data reduction software (Andrews, 2003) referred to below as the 'Yale pipeline.' Each of the CCDs is treated as a separate instrument during reductions. I will therefore explain the procedure only for a single chip. The software first performs the basic bias subtraction and flat-fielding. The bias level for a given column of the CCD is computed by median-combining 25 rows in the overscan region. Dark subtraction and flat-fielding cannot be carried out using the standard techniques of pointed observations. Instead, skyflat and dark driftscans were taken on the first night of observations in both regions. Each such scan is first divided into 240 separate 600 $\times$ 10 pixel segments. These segments are median-combined using the IRAF IMSUM task to remove cosmic rays (darks) or stars (skyflats). The resulting 600x10 pixel image is then averaged into a single row of 600 pixels using the IRAF BLKAVG task. The averaged dark and flat rows are subtracted and divided respectively from each row of data.

For a given CCD, the Yale pipeline divides a drift scan into discrete frames 2048 pixels in length. After pre-processing, the pipeline generates a point-spread function (PSF) for each frame which it uses to detect sources and generate PSF photometry. It registers detections from all four filters and generates an astrometric solution from the USNO-A2 catalog. The Yale pipeline then measures aperture photometry for all objects through a square aperture of half-width 3.5 pixels. The final data product I received was a catalog containing positions and instrumental magnitudes (both PSF and aperture) for each source detected in this manner.

2.2 Post-"Yale Reduction Pipeline" Pipeline

My first task on this project was to build a database to hold the data given to me, some 200 million detections from ∼400 deg^2 of sky. Thus, in total, the Yale catalogs contained ∼440,000 detections per deg^2 or 120 detections per arcmin^2 down to a magnitude of ∼20 (see §2.3 for more details). To put this number into perspective, the Hubble Deep Field detected ∼230 objects per arcmin^2 to a magnitude of ∼30, 13× fainter than my survey limit. As I quickly figured out, the source of the anomalously high number of objects detected in my data largely originated from the methods employed during initial processing of the driftscans. The Yale pipeline is efficient at processing a very large amount of data relatively quickly. However, the pipeline is not designed to be efficient at identifying bona fide astronomical sources. Most of the CCDs that comprise the Quest-2 camera are of *engineering grade* rather than science grade. As a result, they have many more cosmetic defects than those used in typical scientific instruments. The Yale pipeline does not sufficiently account for these defects and thus identifies many CCD artifacts as astronomical sources. This problem is compounded by the fact that the detection algorithm was written to find very faint quasars and therefore uses a low detection threshold which identifies even low signal-to-noise detections as candidate sources.

The third, and dominating source of spurious detections requires explanation of the method that is used by the Yale pipeline to detect sources. For a given frame, a PSF is generated by stacking postage cutouts of individual stars. However, because the pipeline does not first reject faint, crowded or false detections, the frame PSFs are often odd-shaped, and do not adequately represent the PSF of the data. Each star on a given frame is fit with this PSF and then subtracted. Any residuals due to imperfect PSF subtraction (most often due to odd PSFs rather than odd data) are then refit and subtracted again. The process repeats until no residuals are left. Thus, this process produces not only (often) erroneous PSF photometry, but also many extra detections for each star. The combined result of these decisions is that the data catalogs I received were dominated by 'junk' detections, i.e., catalog entries that did not correspond to real sources. The majority of the extra sources originated from single stars that the pipeline decided were two (or more depending on the brightness of the star).

None of the above facts are documented, and thus, it took a non-trivial amount of time (on the order of 6 months) to determine 1) that most of the sources in the catalog were not real, and 2) from where the false detections originated. Once both of these facts had been established, the question became how to get around the problem. The Yale pipeline establishes a detection in one filter and then forces photometry in the other three, regardless of whether the original source is a bona fide star as opposed to a 'junk' source or an artifact. Thus, requiring detections in multiple filters as a way to weed out junk sources at this stage was not effective. Instead, I took advantage of the fact that repeated monitoring observations were taken.

2.2.1 Source Matching

In sum, I took 12 scans of the entire survey field near Taurus, and 24 scans of the central $\sim$60 deg^2 of the field in USco, where one 'scan' refers to a single driftscan observation of the area. I matched detections between scans within a 0.8" radius and computed new coordinates for each source by averaging together coordinates from individual scans. The typical astrometric RMS deviation about the mean was $\sim$0.13". For occasions where multiple sources were detected within a single scan, the source closest (in RA and DEC) to detections of the same star in other scans was chosen as the real source and a 'confusion' flag was inserted into the catalog indicating that the source was either a projected multiple ($a \lesssim 110$ AU in projected distance), or adjacent to one or more bogus detections. This step produced catalogs containing ~8 and ~15 million sources in USco and Taurus, respectively. Of those, ~60% in each region of multiple observations were single detections with no counterparts on other scans and were eliminated from further consideration.

2.2.2 Calibration to the Sloan System

Deriving calibrations capable of converting the Quest-2 photometry to a standard system is significantly more complicated that it is for general point and track observations taken with single CCD cameras. Because the data are taken in driftscan format, the flux from each star has traveled across 2400 separate pixels on a given CCD before being read out. Because each CCD functions as an independent detector, calibrations must be derived for each of the 112 CCDs separately. Many of the CCDs have been found to be highly non-linear, and spectral response is known to vary from pixel-to-pixel across each detector. Both gain levels and linearity have been found to vary as a function of time. Thus, in order to calibrate the data in a truly robust manner, observations of standard stars would need to have been taken at several places on each of the 112 CCDs throughout my observations. Taking such observations was not realistically feasible. Below I describe the procedure I used to calibrate the Quest-2 data to a photometric system *close to* that used by the Sloan Digital Sky Survey (York et al., 2000). I chose to calibrate to Sloan data because, at the time, it was the largest optical imaging survey that significantly overlapped area surveyed with the Quest-2 camera. However, because the calibration data was not observed at the same time as was my survey data (see below), and the gain and linearity are known to be time variable, it is not possible to transform the Quest-2 magnitudes exactly into Sloan photometry.

I matched a subset of data taken by the Quest-2 collaboration (Rabinowitz et al., 2003) in a different part of the sky ($-2.5^o \lesssim \delta \lesssim 2.5^o$, $120^o \lesssim \alpha \lesssim 240^o$) to data from

Sloan. For each of the Quest-2 CCDs, I computed a conversion from Quest-2 to Sloan magnitudes in the form of:

$$r = a_R + b_R \times R_{Quest} + c_R \times Row + d_R \times (R - I)_{Quest}$$

$$i = a_I + b_I \times I_{Quest} + c_I \times Row + d_I \times (R - I)_{Quest}$$

$$g = a_B + b_B \times B_{Quest} + c_B \times Row + d_B \times (B - R)_{Quest},$$

where a_X, b_X, c_X, d_X are constants and '*Row*' refers to a row of pixels (perpendicular to the drift scan direction) on the CCD. Only stars with both Sloan and Quest-2 photometric uncertainties of < 0.1 mag, and instrumental Quest-2 magnitudes 11.5 $< R, I < 19$ and $14 < B < 21$ were used to derive the calibrations to avoid saturated and faint sources with systematically larger uncertainties than those present for the bulk of the population. Constants were computed every 0.75 mag (b_X), 50 pixels (c_X) and 0.2 mag in color (d_X) and determined in an iterative manner for each equation above until each constant changed by <0.0005 mag for at least 3 iterations.

Derived coefficients are shown in figures 2.2–2.8. Many CCDs do not have calibrations either because that CCD is not functioning properly, or because the corresponding CCD required to compute color terms is not functioning properly. Figure 2.2 shows the zeropoint applied to the transformations for each chip plotted as a function of instrument column (i.e., 1–28). Each filter (i.e., row 1–4) is shown as a different symbol. Zeropoints (a_X terms) are negative for all CCDs discussed here. Figures 2.3 & 2.4 illustrate that most CCDs are not linear (b_X coefficients) and CCD sensitivity is a function of magnitude that decreases for brighter stars. Row (pixel on the CCD) coefficients (c_X; figures 2.5 & 2.6) in general are not large. The 'wave-like' pattern seen for CCDs in column 14 occurs because the each filter is actually in parts, which join in the middle of the CCDs in column 14. By far the largest and most structured calibration terms are the color coefficients (d_X) shown in figures 2.7 & 2.8. These figures illustrate that the reddest stars are systematically fainter than the bluest stars by as much as 0.5 magnitudes.

Average values for each constant are given in the second column of table 2.1, along with the full range covered by all 28 CCDs in a particular filter (column 3 of table 2.1). Constants listed correspond to coefficients in the calibration equations given above.

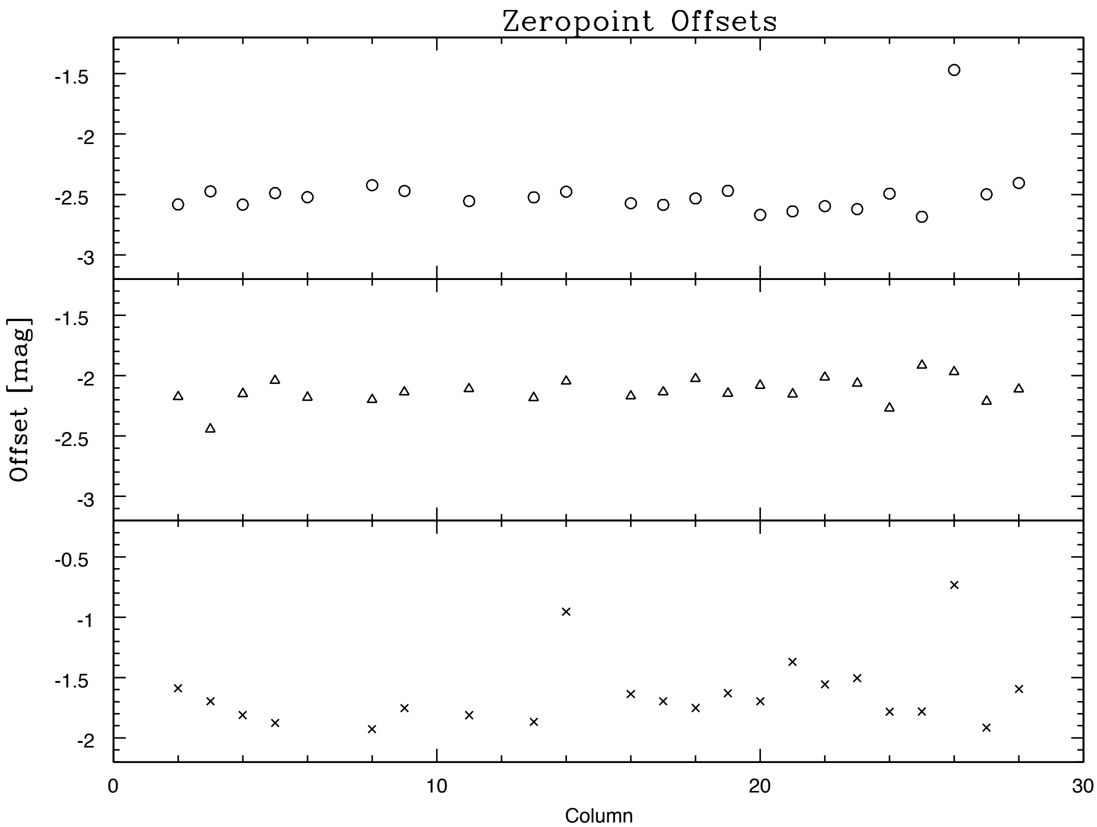

Figure 2.2 Calibration terms (a_X values) shown for individual CCDs, plotted as a function of instrument column (i.e., 1–28). Each filter (i.e., row 1–4) is shown as a different symbol. Symbols are as follows: circles represent R–band terms, triangles represent I–band terms, and x's represent B–band terms. Many CCDs do not have calibrations either because that CCD is not functioning properly, or because the corresponding CCD required to compute color terms is not functioning properly.

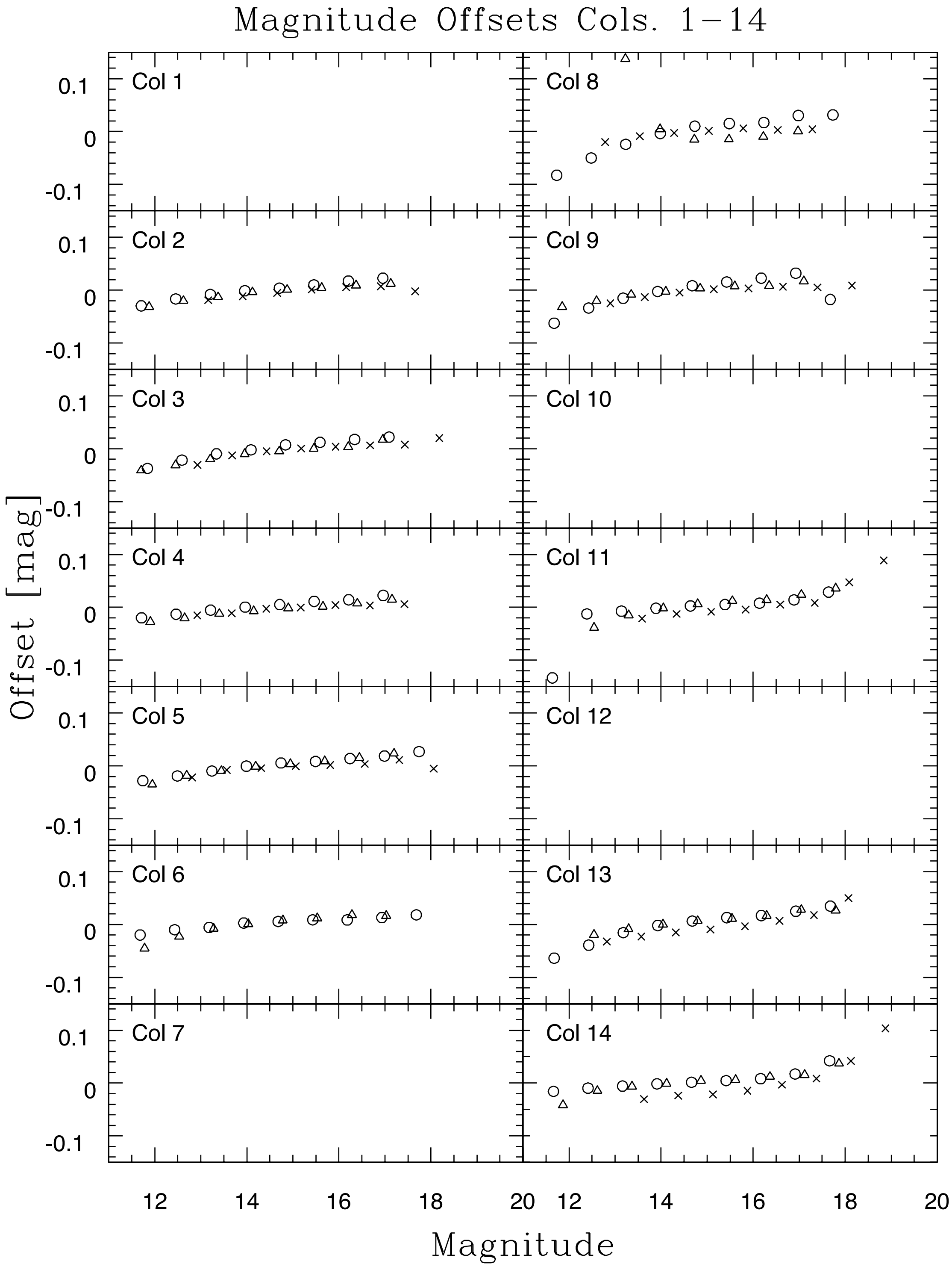

Figure 2.3 Calibration terms (b_X values) for each column (1–14) computed as a function of magnitude. Symbols are as follows: circles represent R–band terms, triangles represent I–band terms, and x's represent B–band terms. Many CCDs do not have calibrations either because that CCD is not functioning properly, or because the corresponding CCD required to compute color terms is not functioning properly.

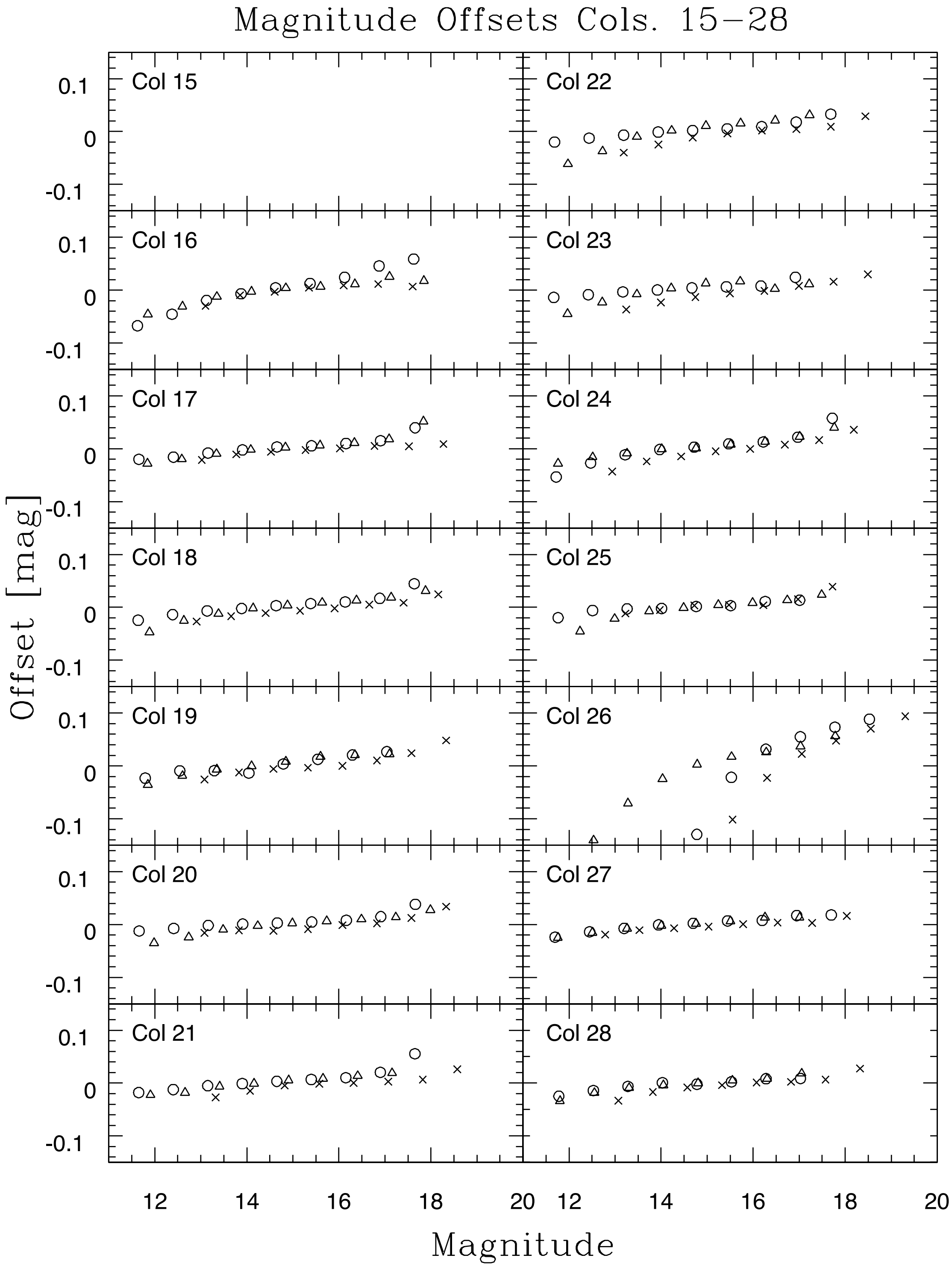

Figure 2.4 Calibration terms (b_X values) for each column (15–28) computed as a function of magnitude. Symbols are as follows: circles represent R–band terms, triangles represent I–band terms, and x's represent B–band terms. Many CCDs do not have calibrations either because that CCD is not functioning properly, or because the corresponding CCD required to compute color terms is not functioning properly.

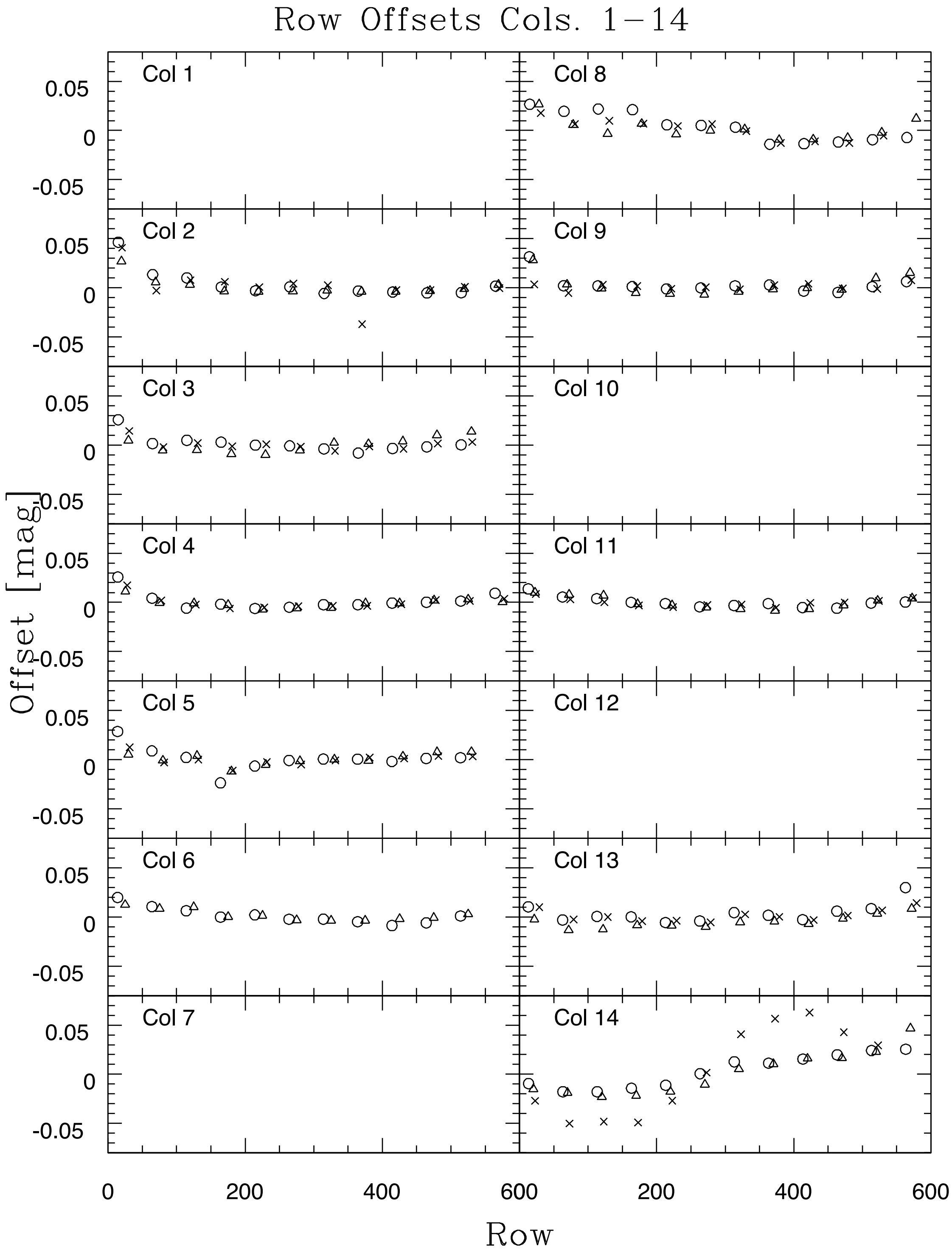

Figure 2.5 Calibration terms (c_X values) for each column (1–14) computed as a function of position on the CCD (i.e., row 0–600). Symbols are as follows: circles represent R–band terms, triangles represent I–band terms, and x's represent B–band terms. Many CCDs do not have calibrations either because that CCD is not functioning properly, or because the corresponding CCD required to compute color terms is not functioning properly.

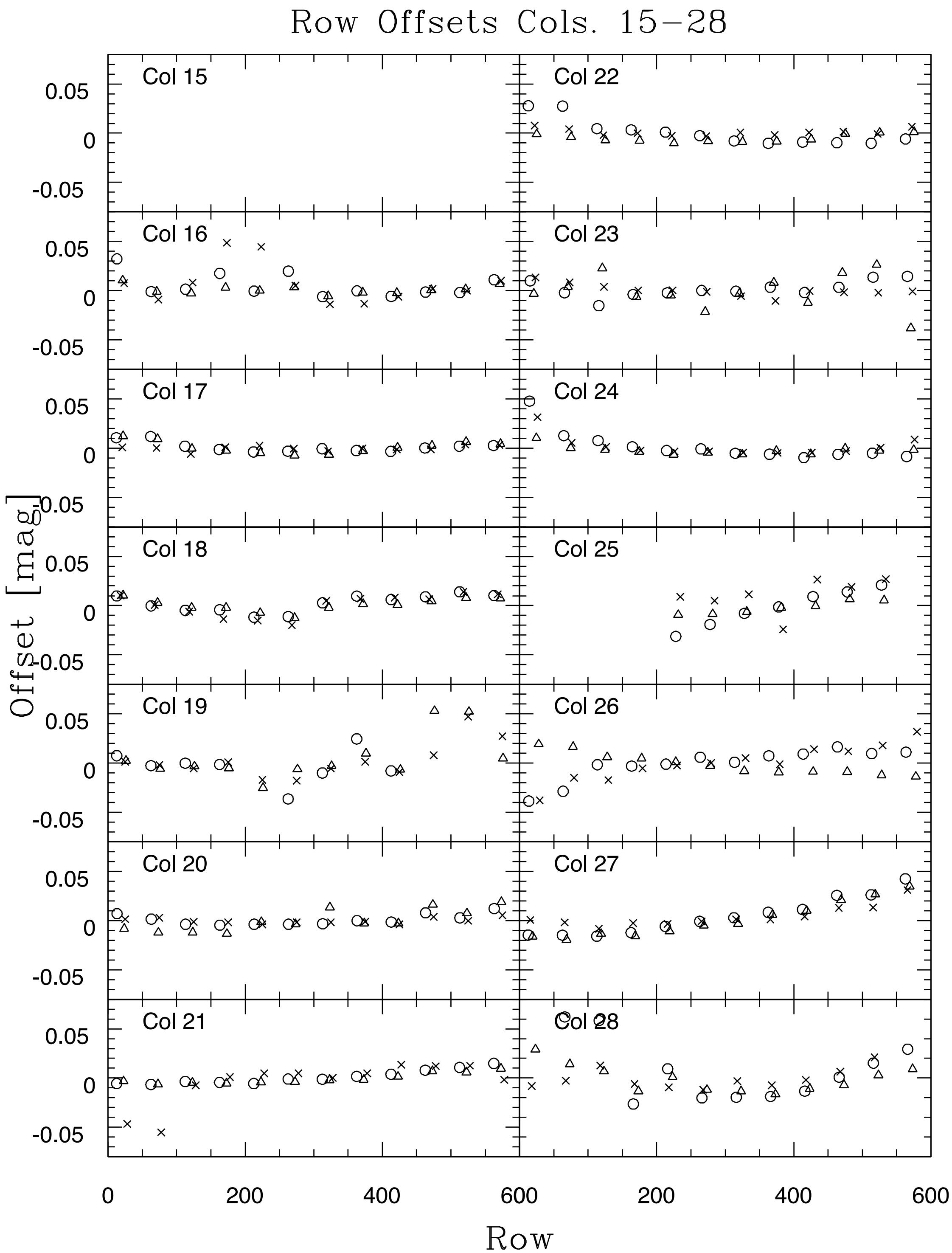

Figure 2.6 Calibration terms (c_X values) for each column (15–28) computed as a function of position on the CCD (i.e., row 0–600). Symbols are as follows: circles represent R–band terms, triangles represent I–band terms, and x's represent B–band terms. Many CCDs do not have calibrations either because that CCD is not functioning properly, or because the corresponding CCD required to compute color terms is not functioning properly.

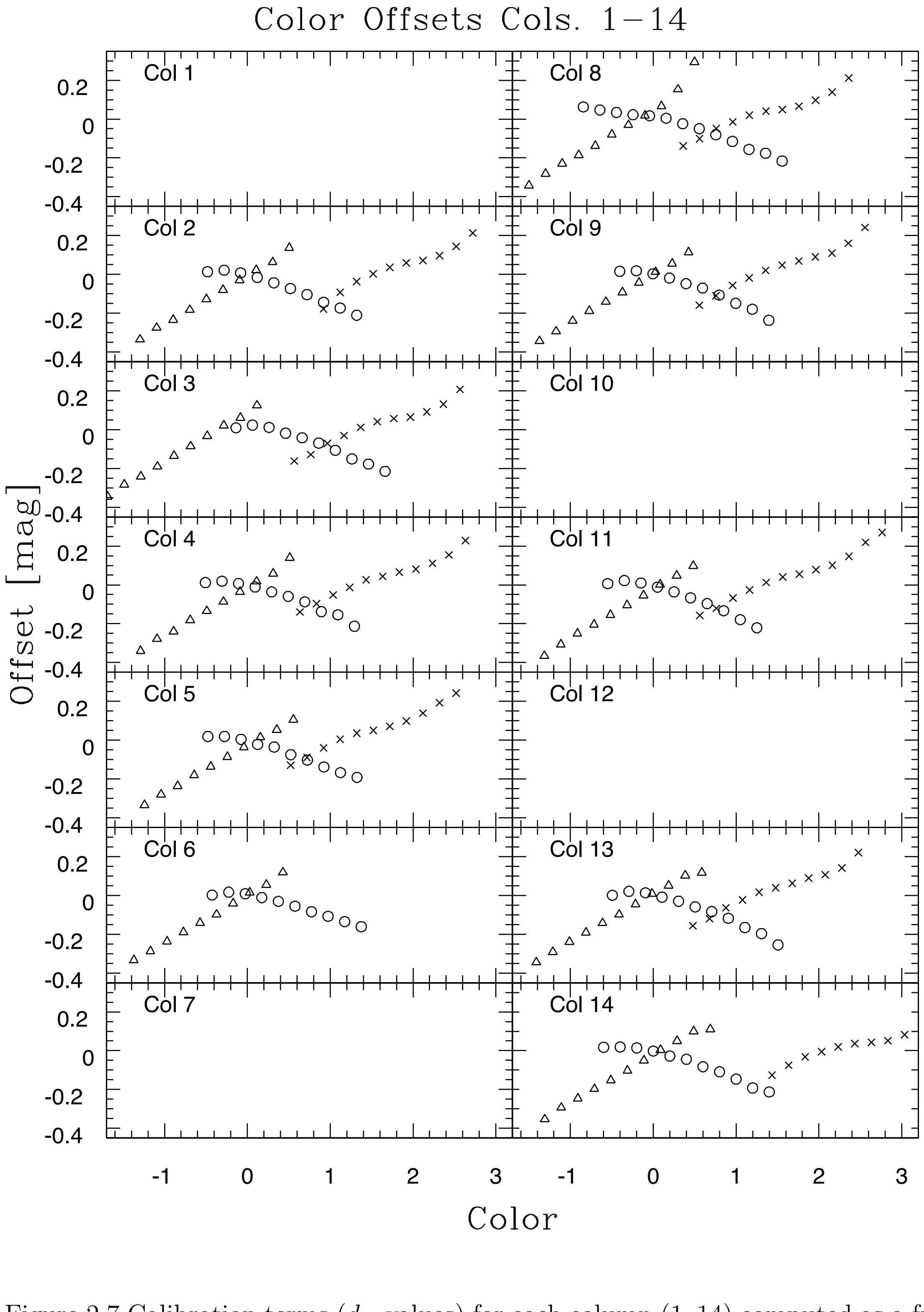

Figure 2.7 Calibration terms (d_X values) for each column (1–14) computed as a function of color. Symbols are as follows: circles represent R–band terms computed from $R-I$ colors, triangles represent I–band terms computed from $I-R$ colors, and x's represent B–band terms computed from $B-R$ colors. Many CCDs do not have calibrations either because that CCD is not functioning properly, or because the corresponding CCD required to compute color terms is not functioning properly.

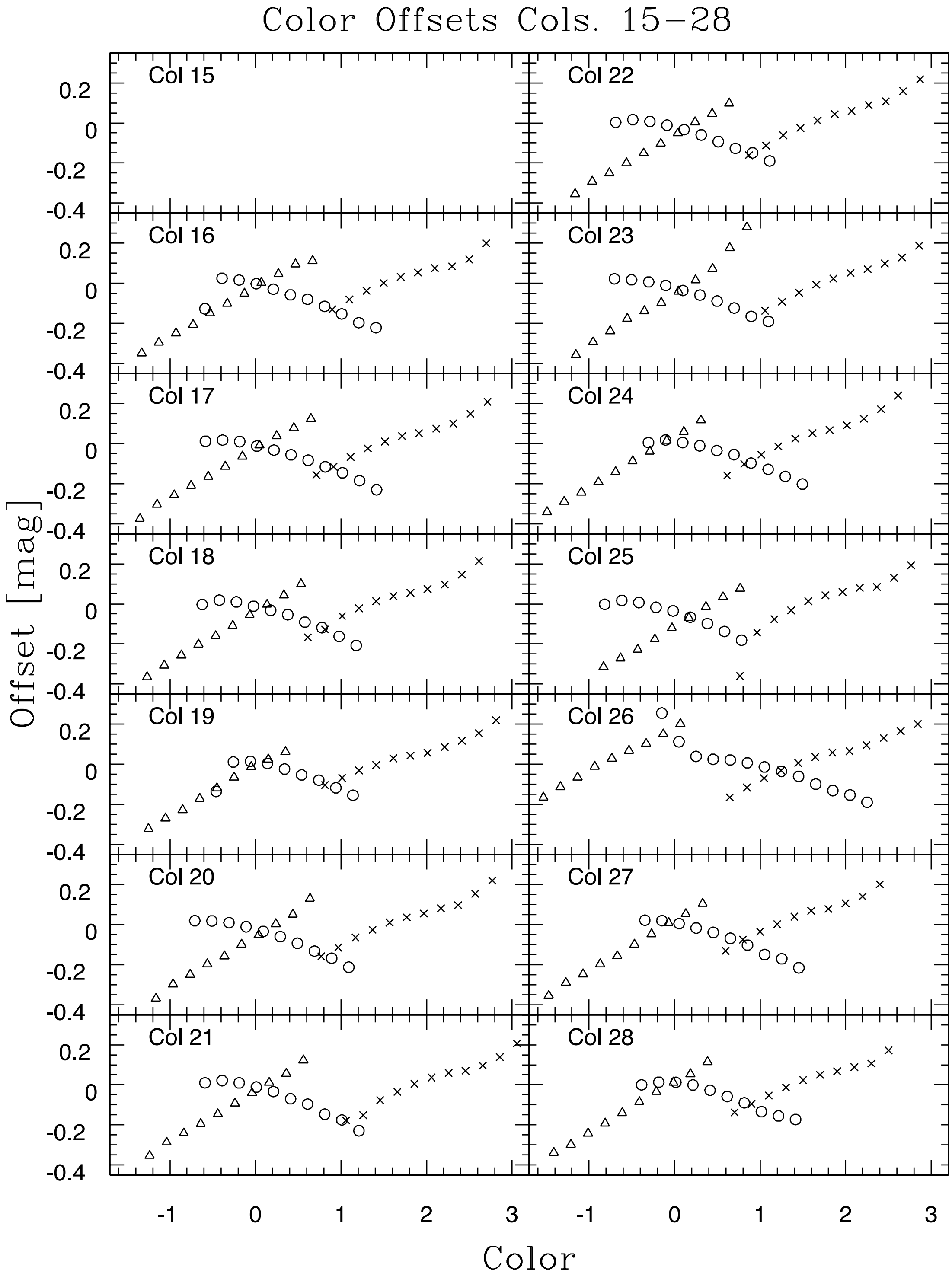

Figure 2.8 Calibration terms (d_X values) for each column (15–28) computed as a function of color. Symbols are as follows: circles represent R–band terms computed from $R-I$ colors, triangles represent I–band terms computed from $I-R$ colors, and x's represent B–band terms computed from $B-R$ colors. Many CCDs do not have calibrations either because that CCD is not functioning properly, or because the corresponding CCD required to compute color terms is not functioning properly.

Table 2.1. Calibration constants for Quest-2–to–Sloan conversions

constant	<value>[a]	full range[a,b]	$< \sigma >$[a]	<nstars>
a_R	-2.49	-2.68 – -1.46	0.06	14717
a_I	-2.12	-2.44 – -1.91	0.05	14735
a_B	-1.63	-1.92 – -0.73	0.06	8933
b_R	-0.01	-1.03 – 0.08	0.13	1653
b_I	0.00	-0.34 – 0.25	0.11	1708
b_B	0.00	-0.54 – 0.10	0.10	1121
c_R	0.00	-0.08 – 0.25	0.13	1234
c_I	0.00	-0.03 – 0.05	0.11	1238
c_B	0.00	-0.05 – 0.06	0.08	753
d_R	-0.06	-0.25 – 0.25	0.14	1399
d_I	-0.10	-0.37 – 0.42	0.10	1408
d_B	0.02	-0.72 – 0.26	0.09	802

[a]Value given is in magnitudes.

[b]'Full range' refers to the minimum and maximum value of each coefficient across all 28 CCDs within a given filter.

Often the range for a single coefficient is quite large, ∼0.5–1 mag, even when the average term is close to zero. This point is illustrated explicitly in figures 2.2–2.8. Also given in table 2.1 is the average sigma for each constant and the average number of stars that went into computing a given constant. In general, average sigmas listed are representative of all CCDs excepting the R & B CCDs in column 26 for which an unreliable cable causes inconsistent measurements and large non-linearity problems.

I applied the derived calibrations to the Taurus and USco instrumental magnitudes by linearly interpolating between values in each parameter for the appropriate CCD's coefficients. Outlier calibration points arising from noisy data at faint magnitudes or chip edges were identified and not applied to the catalog data. To account for differences in airmass between the Yale calibrator scans and USco scans, I applied the first order linear extinction terms as derived by Fukugita et al. (1996), 0.09, 0.08, & 0.18 for rig respectively, and assumed an average airmass of $Z = 2$ for all USco driftscans. The Taurus scans were taken at low air mass similar to that of the calibrator scans, and no airmass correction was applied.

2.2.3 Night-to-Night Calibrations

I accounted for small atmospheric transparency changes during the night and between nights by applying a photometric offset to every scan in both regions as a function of RA. In Taurus, the data were taken primarily under non-photometric conditions. Thus, because some of the data were taken through thick clouds ($\geq$2 mag of extinction), most faint sources were not detected in all 12 scans. In Taurus, I thus chose the 'best' (i.e., most photometric) scan, taken on 27 Nov 2003, to define the photometric reference system. I selected a subset of $\sim$100,000 stars from the source catalog that were detected in at least 6 of 12 scans (including the 'best' scan used as a reference) and had no neighbors within 5". For each such star I computed the difference between the reference magnitude and the magnitude measured in an individual scan. The data in USco were taken under good conditions. Here, I selected a subset of calibrator stars from the source catalog that were detected in at least 20 out of 24 of the monitoring scans, and had no neighbors within 5". For each star and filter an average magnitude of all detections was calculated along with the difference between that average magnitude and the magnitude measured on each individual scan.

In both regions, for every chip and scan I created a catalog of offsets by stepping through in RA every 25 (USco) or 5 (Taurus) calibrator stars and calculating a median offset value. An example is shown in figure 2.9. Due to the highly structured nature of transparency changes that occurred while the Taurus data were taken, it was necessary to compute a finer grid of offsets. Average scan-to-scan offset values for a single CCD were 0.23 mag in i, 0.20 mag in r, and 0.10 mag in g in Taurus, and were much lower ($\pm$0.001 mag in all three filters) in USco. The average range of offsets within a single CCD-scan combination were 1.07 mag in i, 1.23 mag in r, and 1.11 mag in g for Taurus, and 0.05 mag in i, 0.07 mag in r, and 0.07 mag in g for USco. I applied these offsets to the entire dataset as a function of RA and CCD chip by linearly interpolating between values in RA. Because the data span $\sim$5 deg in Dec

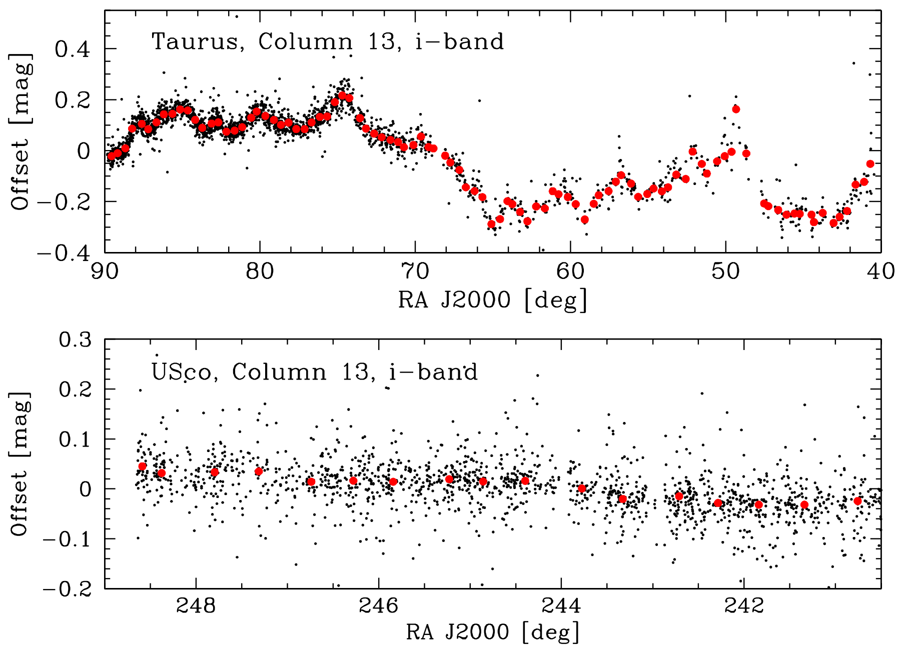

Figure 2.9 Example of calibrations computed to account for transparency changes during the night and from night to night. In both panels, black points represent stars extracted from the catalog meeting the selection criteria outlined in §2.2.3. Large red points represent median values computed every 25 (USco) or 5 (Taurus) stars. Due to the highly structured nature of transparency changes that occurred while the Taurus data were taken, it was necessary to compute a very fine grid of offsets in this region.

per driftscan, offsets as a function of declination were also computed. However, upon examination, I found no systematic structure in the offsets as a function of declination and thus, only the RA offset was necessary.

The high (δ =-15.7^o) and low (δ =-23.3^o) declination scans in USco do not have repeated observations and overlap only the top and bottom 0.8 deg of the monitoring (repeated) scans (δ =-19.5^o) in that region. For these driftscans I calculated a scan offset as a function of RA using the same procedure outlined above but averaging together all columns of overlap with the mid-declination scans, rather than chip by chip. I find this procedure to produce magnitudes consistent with those derived from the multiple-scan region at the $< \Delta mag >$ = 0.2% (r), 0.03% (i), and 3.8% (g) levels for objects in the overlap region. The observed differences in $< \Delta mag >$ between the three filters directly correlates to the observed differences in the average matched magnitude; i.e., the average matched g magnitude is ∼1 mag fainter than the average matched i magnitude, and thus, $< \Delta g >$ is systematically larger than $< \Delta i >$.

2.3 Precision, Accuracy, and Completeness

For each source in the Taurus region and in the central declination strip in the USco region, final stellar magnitudes were computed by averaging together calibrated, transparency-corrected instrumental magnitudes corresponding to the same source on-sky. I can thus use photometry from the monitoring scans to assess the relative precision of the photometric data by computing for each star the RMS deviation of individual measurements about the final, averaged magnitude. I find the photometric precision to be highly CCD dependent, owing to the fact that the 112 CCDs are of varying quality. In the left panels of figure 2.10, I show computed RMS deviations as a function of magnitude in the USco region for four different CCDs. In each plot, RMS data is shown for any star that was detected in more than half of the monitoring scans, i.e., more than 12 times. The top left panel shows repeatability for one of the best CCDs, which have average RMS values from ∼0.02–0.03 mag for stars brighter than gri ∼18, to ∼0.08 mag for stars fainter than this value (i.e., 18 to ∼20–21 mag).

The second panel from the top represents repeatability for a CCD of typical quality, with similar average RMS values of ∼0.02–0.03 mag at the bright end but higher average values of ∼0.09–0.1 at the faint end. I find nine CCDs to be of poor quality with average RMS values of ∼0.12–0.18 for faint stars. An example of such a CCD is shown in the third panel from the top. The bottom panel shows repeatability for one CCD within an anomalous column that is known to produce highly unstable magnitudes. The corresponding panels on the right show data taken on with the same CCDs in the Taurus survey for stars observed in at least half (>6) of the scans in that region. Due to bad weather at the time these data were taken, the data are of poor repeatability even after calibration, but could possibly be used to identify very high amplitude variables.

Figure 2.11 shows the similar data to that shown in the left panels of figure 2.10, but for $r - i$ color. In this case the data represent the difference of magnitudes from two different CCDs within a column. I find both color repeatability and the distribution of observed colors to be highly column dependent, as would be expected given the differences observed between CCDs in figure 2.10.

The accuracy of the absolute photometry is harder to quantify. While I have accounted for relative extinction due to weather within the dataset, I am not able to account for zero point shifts between the Taurus/USco drift scans and the scans used to derive the Quest-2–to–Sloan calibrations. Despite this fact, comparison of the average $r - i$ color for the calibrated Quest-2 photometry agrees to ∼0.01 mag with the average $r - i$ color of the Sloan data used to derive the calibrations. Therefore, while I cannot claim the photometry is on a standard Sloan g, r, i system, it should be fairly closely aligned with Sloan.

From histograms of all detections (figure 2.12) for the rig filters, I find a peak in number of objects detected at $r \sim 20$ mag, $i \sim 19.5$ mag, and $g \sim 20$ mag for the USco data. In Taurus, my photometric survey was slightly shallower (by ∼0.5 mag) due to challenges produced from bad weather. Figures 2.13–2.15 show detection histograms of each CCD individually for data taken in the USco region. The completeness turnover for all CCDs as an ensemble within the row containing

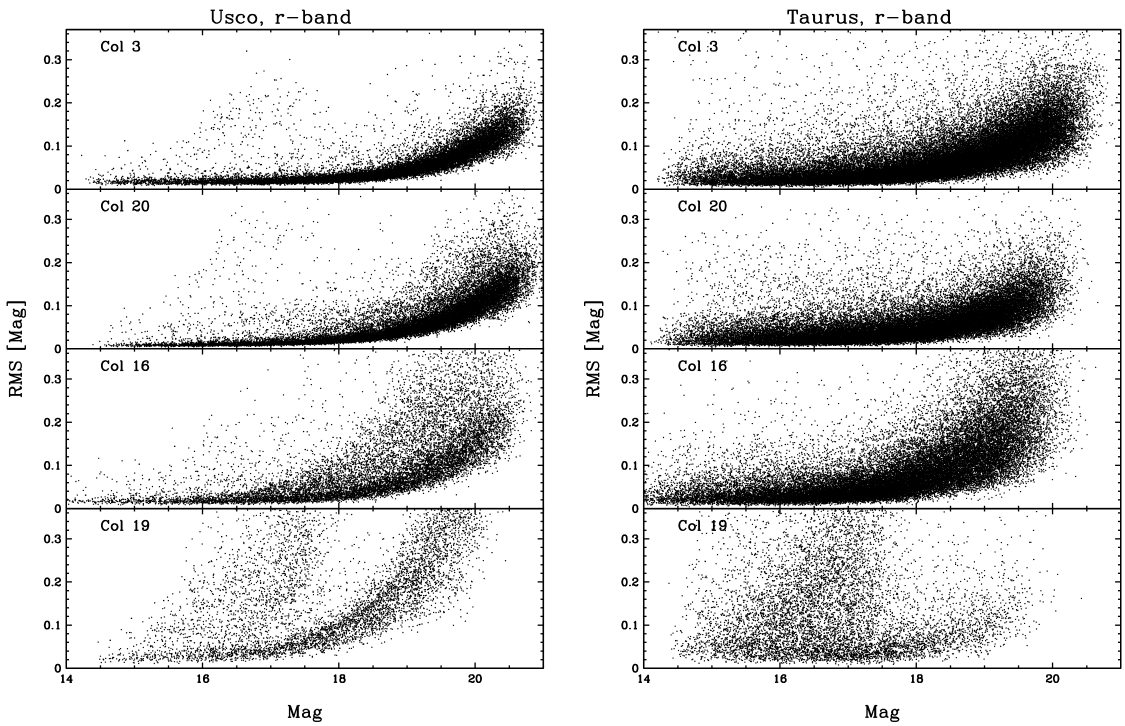

Figure 2.10 Panels on the left show computed RMS deviations as a function of magnitude in the USco region for four different CCDs. RMS data is shown for any star that was detected in more than half of the monitoring scans, i.e., more than 12 times. Each magnitude is the average of all measurements and the corresponding RMS values represent the deviation of individual measurements about that average. The top left panel shows repeatability for one of the best CCDs, the second panel represents repeatability for an average CCD, and the third panel from the top shows repeatability for one of the worst CCDs. The bottom panel shows repeatability for one CCD within an anomalous column that is known to produce highly unstable magnitudes. The corresponding panels on the right show data taken on with the same CCDs in the Taurus region. Due to bad weather at the time these data were taken, the data are of poor repeatability even after calibration.

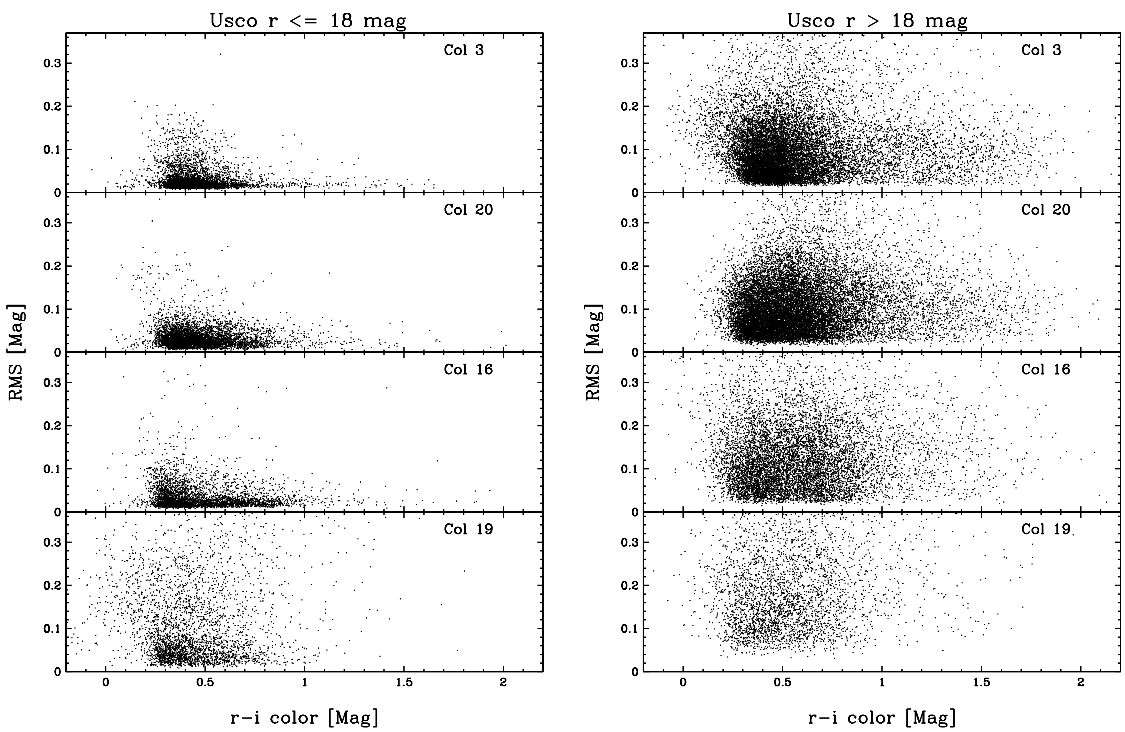

Figure 2.11 Computed RMS deviations as a function of $r - i$ color in the USco region for bright (left panel) and faint (right panel) stars in four different columns. RMS data is shown for any star that was detected in more than half of the monitoring scans, i.e., more than 12 times in both r and i CCDs within a column. Each magnitude is the average of all measurements and the corresponding RMS values represent the deviation of individual measurements about that average. Panels are as described in figure 2.10.

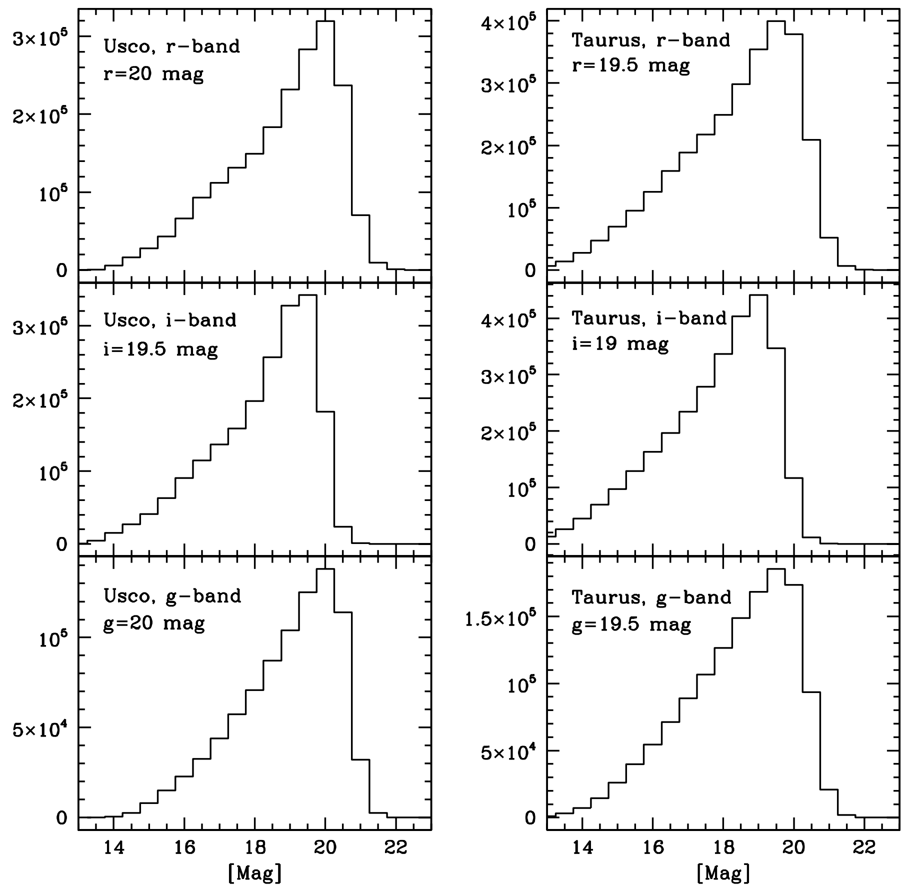

Figure 2.12 Number of individual stars in each region as a function of magnitude. Data have been binned by 0.5 mag. Approximate histogram peaks are given in each panel.

that CCD (i.e., all 28 columns in a single filter) is shown in each panel as a dotted line. Data in figures 2.12–2.15 have been binned by 0.5 magnitudes. The histogram peak, saturation points and CCD sensitivity varies between CCDs. However, in general, I find the peak of the histograms for individual CCDs corresponds to that found for the ensemble average in that filter. Noted exceptions are that CCDs in columns 19 and 25 (in all filters) and column 16 in the g filter are not as sensitive as most of the other CCDs, due to electronic/detector unreliability, and the histograms for CCDs in column 26 (all filters) have a different profile shape than most others. The histograms for the r and i CCDs in column 28 have the same shape as for the other r and i CCDs, however, many fewer sources were detected.

2.4 Summary of Quest-2 Photometric Survey

The final source catalogs contains optical photometry for $\sim$3 million sources within the $\sim$250 deg^2 Taurus survey region and $\sim$2 million sources in the $\sim$150 deg^2 USco region. In both regions, some or all of the stars have repeated monitoring observations. In this chapter I detail source matching among the repeated observations and account for night-to-night transparency changes. I also convert the data such that they are closely aligned with the standard Sloan gri system. In the next chapter (chapter 3), I present photometric diagrams (color-color and color-magnitude), and explain how I use these data combined with follow-up spectroscopic observations to identify PMS stars.

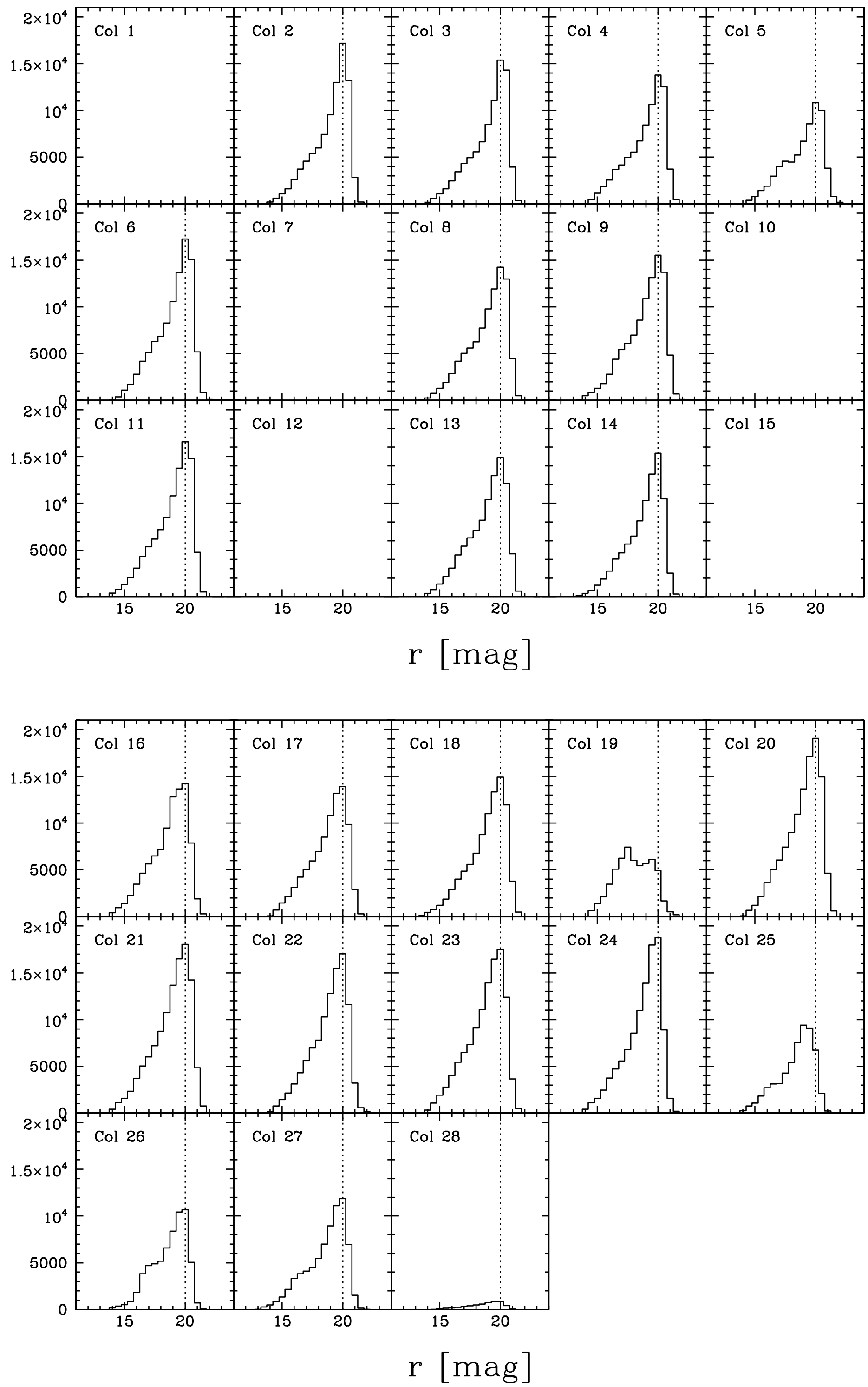

Figure 2.13 Number of detections as a function of magnitude in the USco survey for individual CCDs. The completeness turnover for all CCDs in the r filter as an ensemble is shown in each panel as a dotted line at r=20 mag. Variations in completeness, saturation point, and sensitivity can be seen between CCDs. Blank panels correspond to CCDS that have either failed since installation, or do not have derived calibrations (see §2.2.2).

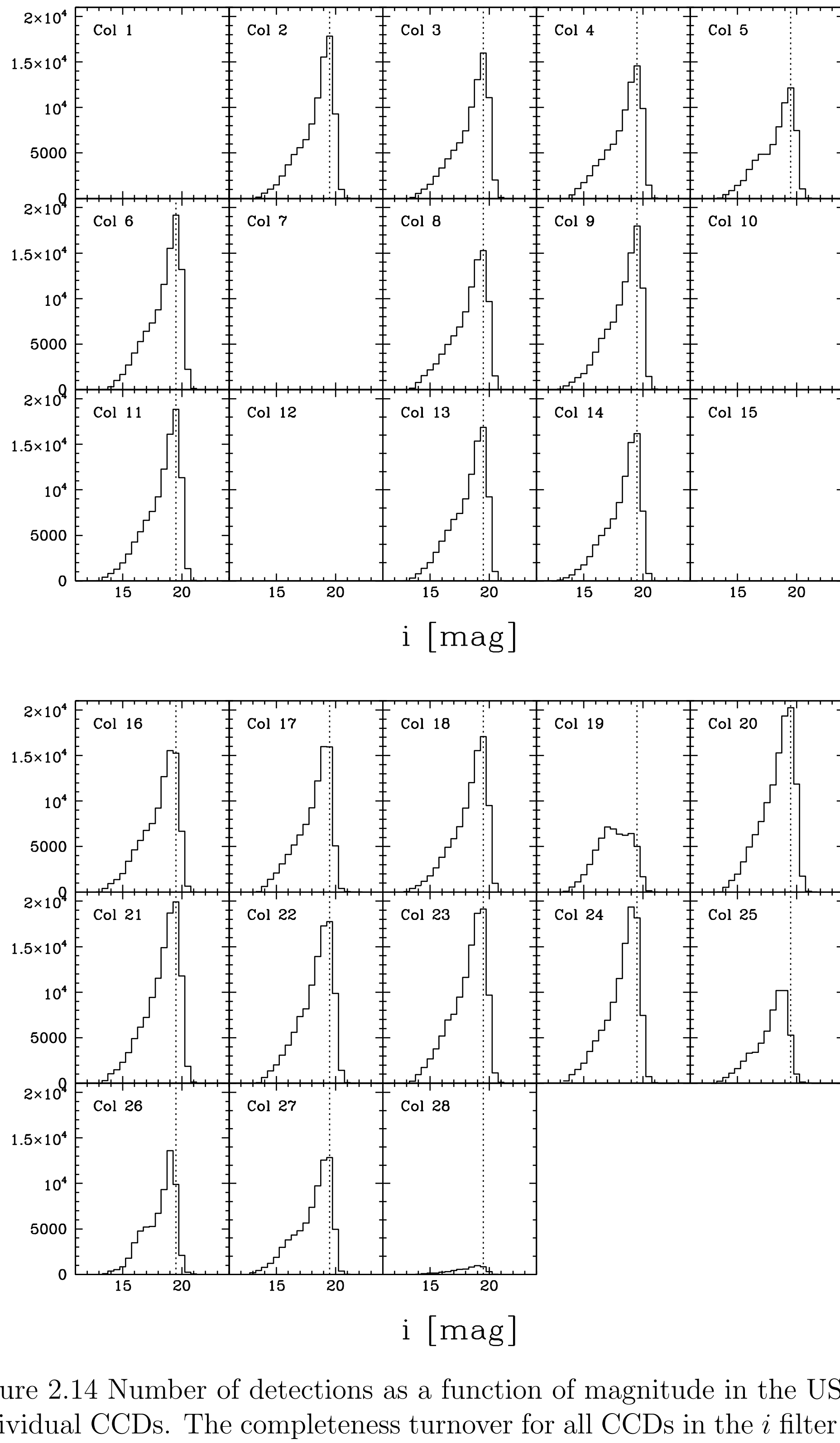

Figure 2.14 Number of detections as a function of magnitude in the USco survey for individual CCDs. The completeness turnover for all CCDs in the i filter as an ensemble is shown in each panel as a dotted line at i=19.5 mag. Variations in completeness, saturation point, and sensitivity can be seen between CCDs. Blank panels correspond to CCDS that have either failed since installation, or do not have derived calibrations (see §2.2.2).

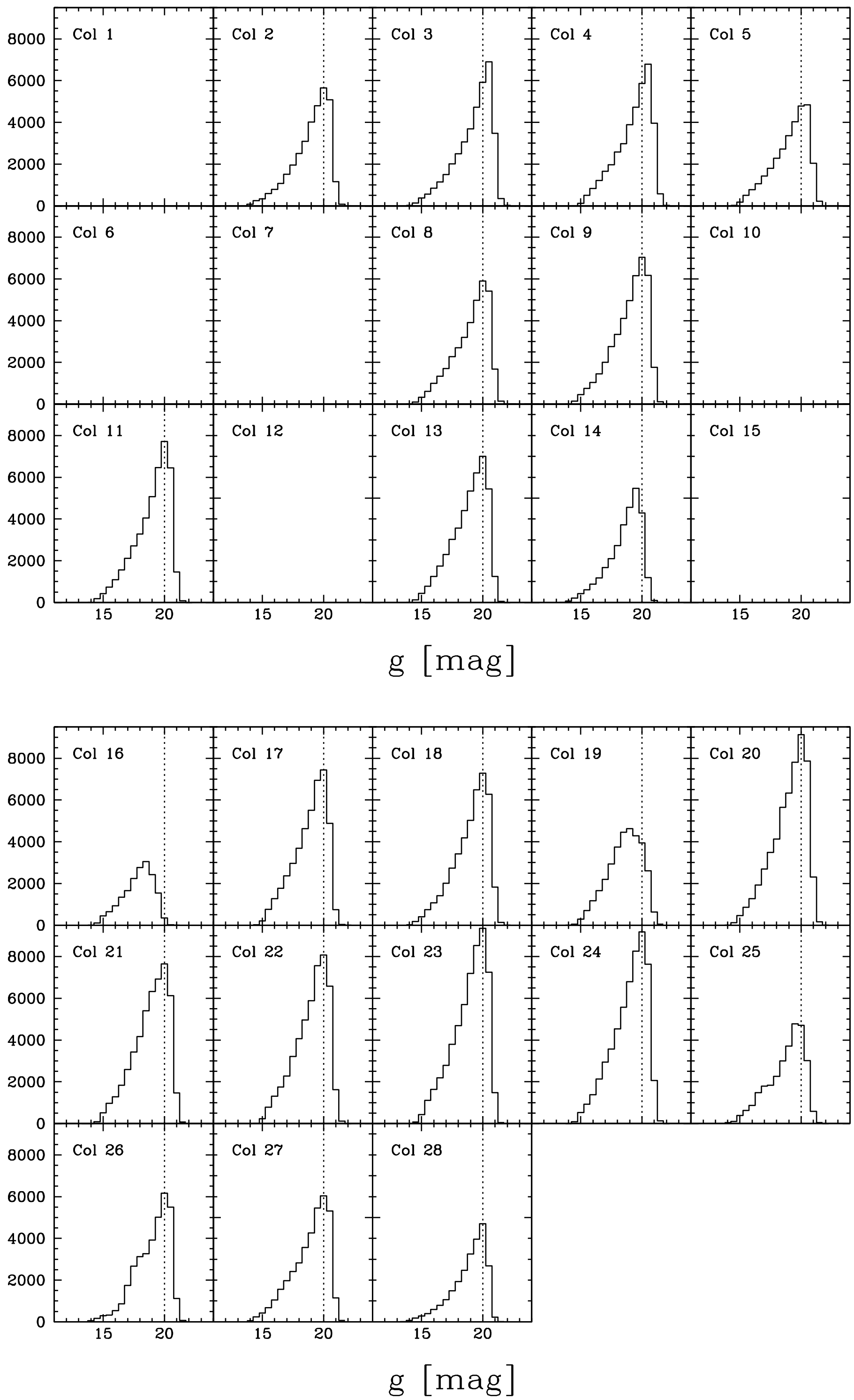

Figure 2.15 Number of detections as a function of magnitude in the USco survey for individual CCDs. The completeness turnover for all CCDs in the g filter as an ensemble is shown in each panel as a dotted line at g=20 mag. Variations in completeness, saturation point, and sensitivity can be seen between CCDs. Blank panels correspond to CCDS that have either failed since installation, or do not have derived calibrations (see §2.2.2).